# Low-symmetry vacancy-related spin qubit in hexagonal boron nitride

Rohit Babar[1,2,†], Gergely Barcza[1,2,†], Anton Pershin[1,†], Hyoju Park[3], Oscar Bulancea Lindvall[4], Gergő Thiering[1], Örs Legeza[1,5], Jamie H. Warner,[3] Igor A. Abrikosov[4], Adam Gali[1,6,*], and Viktor Ivády[2,4,7,8,*]

[1] *Wigner Research Centre for Physics, PO Box 49, H-1525, Budapest, Hungary*

[2] *MTA–ELTE Lendület "Momentum" NewQubit Research Group, Pázmány Péter, Sétány 1/A, 1117 Budapest, Hungary*

[3] *Walker Department of Mechanical Engineering and Materials Graduate Program, Texas Materials Institute, The University of Texas at Austin, Austin, Texas 78712, United States*

[4] *Department of Physics, Chemistry and Biology, Linköping University, SE-581 83 Linköping, Sweden*

[5] *Institute for Advanced Study, Technical University of Munich, Lichtenbergstrasse 2a, 85748 Garching, Germany*

[6] *Department of Atomic Physics, Budapest University of Technology and Economics, Budafoki út 8., H-1111, Budapest, Hungary*

[7] *Eötvös Loránd University, Egyetem tér 1-3, H-1053 Budapest, Hungary*

[8] *Max-Planck-Institut für Physik komplexer Systeme, Nöthnitzer Street 38, D-01187 Dresden, Germany*

†*Contributed equally.*

**email:gali.adam@wigner.hu; ivady.viktor@ttk.elte.hu*

May 12, 2026

**Point defect qubits in semiconductors have demonstrated their outstanding capabilities for high spatial resolution sensing generating broad multidisciplinary interest. Hexagonal boron nitride (hBN) hosting point defect qubits have recently opened up new horizons for quantum sensing by implementing sensing foils. The sensitivity of point defect sensors in hBN is currently limited by the linewidth of the magnetic resonance signal, which is broadened due to strong hyperfine couplings. Here, we report on a vacancy-related spin qubit with an inherently low symmetry configuration, the VB2 center, giving rise to a reduced magnetic resonance linewidth at zero magnetic fields. The VB2 center is also equipped with a classical memory that can be utilized for storing population information. Using scanning transmission electron microscopy imaging, we confirm the existence of the VB2 defect in free-standing monolayer hBN. Our results pave the way for improving the sensitivity of atomic-scale sensing in low dimensions.**

## Introduction

In the new era of quantum sensing, point defect qubits play a crucial role in revolutionizing measurements in material science, biology, and medicine.[1] In particular, the NV center in diamond[2] has provided the means to detect magnetic field[3], electric field[4], strain[5], and temperature[6] with high spatial resolution and high sensitivity. Novel magnetic resonance protocols[7,8] with unlimited frequency resolution[9,10] have opened new horizons for magnetic resonance in the few-spin limit that provides hitherto inaccessible information on the structure and functioning of molecules and proteins[11]. On the other hand, the NV center is an inherently bulk system, that implies severe challenges when near-surface applications are demanded.[?,12] Wide-band gap van der Waals semiconductors with mature exfoliation possibilities, such as hBN, hosting applicable, optically addressable point defect qubits on the surface and even in a single layer may be advantageous in various sensing applications.[13,14] Recently, hBN sensing foils have been utilized to detect the magnetic field of van der Waals heterostructures[15,16], paramagnetic defects[17,18], and other nanometer-scale structures[19].

Optically detected magnetic resonance (ODMR) studies have demonstrated optically addressable spin qubits in hBN.[?,20–23] One of the qubits has already been assigned to the negatively charged boron vacancy ($V_B$ center)[21,24–26]. The VB center can be coherently manipulated[27,28] and used as high spatial resolution thermometer[29] and magnetic field probe[15–19]. The sensitivity of these sensors, however, falls most often behind the NV center in diamond.[30] The reasons for the relatively low sensitivity of the $V_B$ center are the low photon emission rate due to the first-order forbidden optical transition[24] and the noisy environment due to the 100% natural abundance of paramagnetic isotopes of B and N. Other ODMR centers in hBN exhibit narrow linewidth[?,22,23] and bright optical signals, however, their microscopic structures are yet to be explored. While these centers are promising for quantum sensing[?,23], their controlled fabrication on an ensemble level has not been achieved.

Here we experimentally and computationally investigate a point defect complex created by the fusion of two boron vacancies in the neutral charge state. We demonstrate by scanning transmission electron microscopy (STEM) imaging that the stable configuration of the defect, named

VB2 center, can be created in single-layer free-standing hBN samples. We report on nearly degenerate singlet-triplet pairs of states in the spectrum of the defect with allowed optical transitions for initializing and reading out the spin states. We show that the peculiar electronic structure of the VB2 configuration enables long-lived storage of population information in the singlet manifold. Furthermore, we demonstrate that the transverse zero-field splitting interaction of the ground state gives rise to efficient coherence protection mechanisms. As a result, the electron spin resonance linewidth is reduced by a factor of 4.2, and the inhomogeneous coherence time is elongated by a factor of 7.5 at zero magnetic fields compared to those obtained at non-zero magnetic field values. The reported properties of the VB2 center may be utilized in novel quantum sensing applications with high sensitivity.

## Results

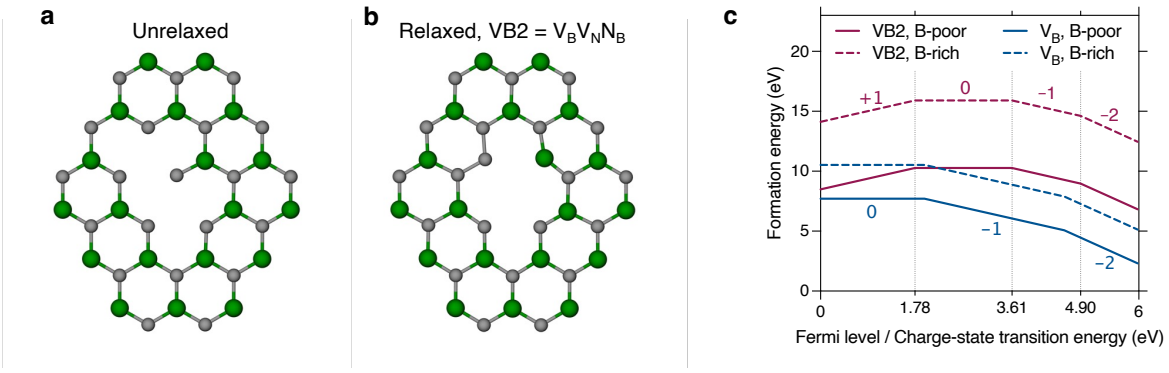


Figure 1: **Structure and stability of the VB2 center.** **a**, Unrelaxed structure of two adjacent boron vacancies. **b**, The energetically most favorable VB2 configuration where the unstable nitrogen atom of two dangling bonds has jumped into the upper boron vacancy site forming a $V_BV_NN_B$ complex. **c**, Formation energies of VB2 (magenta) and $V_B$ (light blue) defects in h-BN as a function of Fermi level under B-poor (solid line) and B-rich (dashed line) growth conditions. Color-coded numbers represent the charge states of the corresponding defect, while vertical dotted gray lines indicate the charge state transition levels of the VB2 defect.

**Structure and stability.** A pair of adjacent in-plane boron vacancies results in a highly unstable configuration where the nitrogen atom between the two vacancies possesses two dangling bonds and binds only to a single boron atom, see Fig. 1a. The loosely bonded nitrogen atom between the boron vacancies migrates into one of the vacancy sites and forms a new point defect complex consisting of a boron vacancy, a nitrogen vacancy, and a nitrogen anti-site ($V_B V_N N_B$), see Fig 1b. The defect complex is hereinafter referred to as the VB2 configuration. Due to the formation of strong nitrogen-nitrogen bonds in the VB2 configuration, the complex is highly favorable. Indeed, the binding energy of two boron vacancy pairs is found to be as large as 5.14 eV.[31]

The formation energy curves of the VB2 and the $V_B$ defects as a function of the Fermi energy are depicted in Fig. 1c. The figure demonstrates that the VB2 configuration exhibits four stable charge states and three charge-state transition levels, $(+1/0)$, $(0/-1)$, and $(-1/-2)$ at 1.78 eV, 3.61 eV, and 4.90 eV in the band gap of hBN, respectively. The neutral charge state is stable in the middle of the band gap and photostable up to 3.61 eV photon energy, which is the threshold for exciting an electron from the conduction band to a defect ionization state, see Fig. 1c.

We conclude from these results that the VB2 configuration may be created in bulk hBN by either electron or neutron irradiation and subsequent annealing at 1000 K. For further details on fabrication, see Supplementary Note 2.

**Excited state properties.** The in-plane and perpendicular-to-plane dangling bonds of the VB2 configuration give rise to a number of localized defect states, most of which can be found in the band gap of hBN. A comprehensive analysis of the single-particle electronic structure can be found in Supplementary Note 3. As a consequence of the complicated electronic structure, several excited states can be found below the ionization threshold resulting in diverse optical excitation and decay pathways.

The energy level spectrum including the eight lowest-lying many-particle energy levels obtained on corresponding relaxed geometries is depicted in Fig. 2a. The spectrum exhibits a peculiar feature that has not been seen in point defect qubits before, i.e. it is built up from nearly degenerate pairs of singlet and triplet states, referred to as excited manifolds from now on. The reason for the

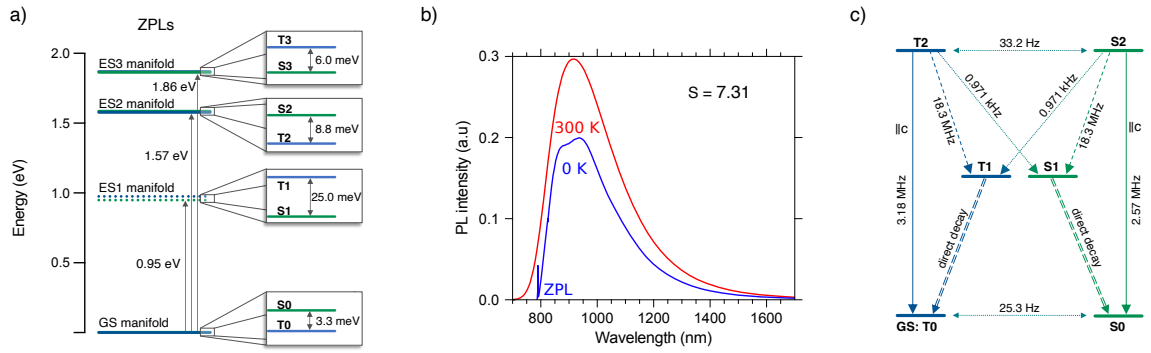


Figure 2: **Optical properties, initialization, and non-destructive readout of the VB2 center. a**, Energy level structure of the VB2 defect exhibiting quasi degenerate singlet-triplet pairs throughout the spectrum. **b**, Calculated PL emission spectra of the VB2 defect a room temperature. The emission maximum is red-shifted by 60 nm compared to the PL emission peak of the $V_B$ center. **c**, Schematic diagram of the possible radiative and non-radiative relaxation pathways. Solid arrows indicate optical transition with parallel to $c$-axis polarization, dashed arrows indicate spin-conserving non-radiative relaxation, dashed double line arrows indicate direct spin-conserving relaxation to the ground state, and dotted arrows indicate spin non-conserving non-radiative transitions through inter-system crossings.

observed quasi-degenerate singlet-triplet pairs can be understood by examining the ground state triplet. Due to the defect's low symmetry, the observed high-spin ground state is the result of an accidental degeneracy in the single-particle electronic structure, see Supplementary Note 3. The unpaired electrons occupy two defect states that belong to two different irreducible representations and are localized on distinct first neighbor atoms of the defect, see the spin density in Fig. 3a. As a result, the exchange energy is marginal in the ground state and gives rise only to a 3.3 meV splitting between the ground state triplet and the corresponding lowest energy singlet state. The wavefunctions of the low energy optical excited states exhibit similar characteristics that explain the spectrum depicted in Fig. 2a.

Since the triplet and singlet states in each manifold have approximately the same spatial

wavefunctions and atomic configurations, spin-orbit coupling and phonon-mediated inter-system crossing (ISC) between these states are forbidden in leading order (El-Sayed's rule). Consequently, the lowest lying S0 singlet excited state close to the triplet ground state T0 is long-lived. Indeed, we find the lifetime of the S0 state to be as long as 39.5 ms at low temperatures, which remains in the same order of magnitude even at room temperature. This indicates that the S0 singlet state can serve as a classical memory to store population information.

By analyzing the potential decay pathways from the excited states, we find that the states in the lowest-lying ES1 manifold can directly decay non-radiatively to the ground state, and its lifetime is expected to be in the picosecond range, see Supplementary Note 4. The fast decay suppresses any optical emission from the T1 triplet and S1 singlet states. On the other hand, the ES2 manifold is optically active and gives rise to zero-phonon luminescence (ZPL) lines from the T2 triplet and the S2 singlet states at 1.578 eV and 1.586 eV, respectively. We note color centers most often emit from the lowest energy excited state, however, depending on the ratio of the radiative and non-radiative decay rates, higher-lying excited states may also be optically active.[32] High-temperature PL spectrum of the VB2 defect is depicted in Fig. 2b showing a 60 nm red-shifted PL phonon side-band compared to the boron vacancy center. The ES3 manifold decays dominantly to the ES2 manifold via non-radiative processes.

Fig. 2c depicts the most relevant radiative and non-radiative decay pathways of the VB2 defect. Besides the optical decay, the system can decay non-radiatively from the ES2 manifold through the ES1 manifold to the ground state manifold. For the quantum efficiency of the VB2 center, we obtain 0.15 and 0.12 for the triplet and the singlet transitions, respectively. The inter-system crossing (ISC) rates between the singlet and triplet channels are a few orders of magnitude smaller than the spin-conserving decay rates, see Fig. 2c. Consequently, the singlet and triplet emissions are independent of each other to a large degree. This effect and the differences in the optical lifetime and the emission energy of the T2 triplet and the S2 singlet states can be utilized to realize a single-shot read-out of the singlet-triplet occupation, see Supplementary Note 4 for more details.

Since the electronic structure of the VB2 configuration does not exhibit dark long-lived

metastable states, the photon count observed in the measurements is limited by the radiative lifetime, two-photon excitation processes, and collection efficiency of the emitted photons in saturation. Due to the high photon collection efficiency achievable in hBN[33,34] and the ≈3 MHz radiative lifetime of the VB2 center, the saturated photo-count of a single VB2 center is expected to be in the order of 100 kcps.

The ISC transition between the singlet and triplet states is found to be strictly selective on the spin sub-levels of the triplet states, i.e. only the $|m_S = 0\rangle$ state is connected with the singlet channel. Consequently, continuous optical excitation of the VB2 center leads to spin polarization in the triplet ground state. Furthermore, since the triplet and singlet radiative relaxation rates are slightly different in the ES2 manifold, see Fig. 2c, the luminescence of the VB2 defect depends on the spin state. The saturated spin read-out contrast is approximated to be 4.6%, see Supplementary Note 4. Since the contrast is set by the relative luminescence intensity of the singlet and triplet manifolds, for which we do not expect considerable temperature dependence, and not by the relative rates of various non-radiative decay processes, the observed 4.6% contrast may be preserved even at room temperature. Finally, we note that fast ISC transitions and fast optical spin initialization may be achieved by pumping through the ES3 manifold, where ISC rates are found in the MHz range. Such excitation, on the other hand, may not be advantageous for read-out due to the enhanced non-radiative decay rates that may substantially reduce the quantum efficiency of the defect.

**VB2 center as a qubit.** As we have shown, the spin states of the ground state triplet of the VB2 center can be initialized and read out optically, therefore the spin states of the defect complex can implement an optically addressable qubit in hBN. In the following, we study the spin and qubit properties of the center. Fig. 3a depicts the spin density of the triplet ground state that clearly shows low symmetric characteristics, in contrast to existing point defect qubits that exhibit (quasi-)three-fold rotation symmetry. The spin Hamiltonian of the triplet ground state is discussed in Supplementary Note 5 in detail.

The low symmetric structure has a significant effect on the zero-field splitting (ZFS) interaction whose preferential quantization axis is in-plane and the corresponding conventional ZFS parameters are $D = 1.394$ GHz and $E = 78.2$ MHz. Note, however, that the preferential quan-

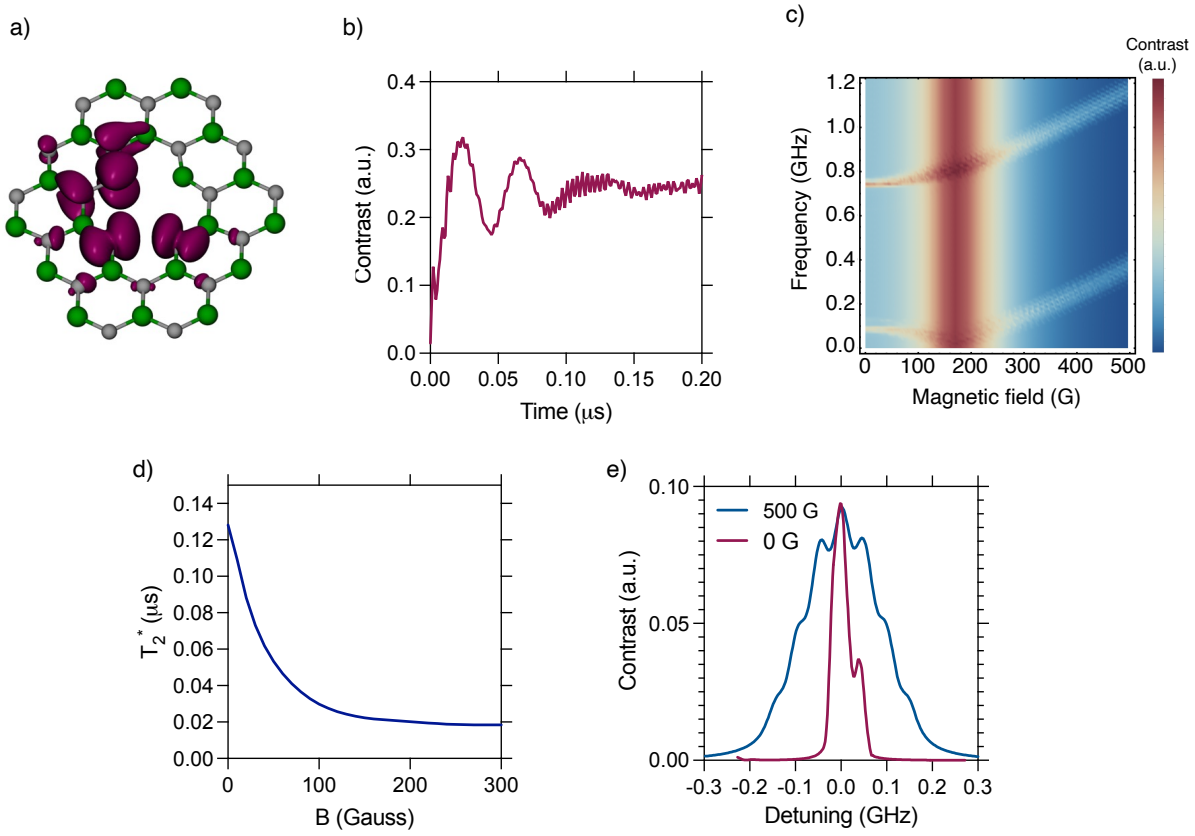


Figure 3: **Qubit properties of the VB2 center.** **a**, Spin density of the triplet ground state of VB2 center. **b**, Rabi oscillation of the electron spin at zero magnetic fields. **c** Magnetic resonance map of the VB2 center as a function of the applied magnetic field (horizontal axis) and the microwave frequency (vertical axis). In the simulations, the system was driven by an in-plane polarized microwave field. The broad frequency-independent signal at 160 G is due to the hyperfine mixing of the spin states observed at the level avoided-crossing of the electron spin levels. **d**, Magnetic field dependence of the free induction decay time ($T_2^\star$). The coherence time is enhanced by a factor of 7.5 close to $B = 0$ due to the transverse zero-field splitting that partially suppresses the hyperfine coupling. **e**, Magnetic resonance signal at 0 G and 500 G magnetic field values. The width of the zero-field electron spin resonance signal is 23.8% of the width of the signal at 500 G. This effect gives rise to a 4.2 times enhancement of the sensitivity at zero magnetic field.

tization axis of the spin-orbit interaction is perpendicular to the plane. Hereinafter, we use this latter quantization axis, in which the electron spin is polarized in the $|m_S = 0\rangle = |0\rangle$ spin state. In this basis, a new set of non-conventional ZFS parameters can be defined as $\widetilde{D} = -814$ MHz and $\widetilde{E} = -658$ MHz that provides the same level structure as the conventional ZFS parameters in the corresponding quantization basis.

The large effective transverse ZFS $\widetilde{E}$ mixes the $|m_S = \pm 1\rangle = |\pm 1\rangle$ spin states and gives rise to new quantum states $|\pm\rangle = |+1\rangle \pm |-1\rangle$. By applying a microwave field that is polarized in an in-plane direction, spin transitions can be resonantly driven between the $|0\rangle$ and $|\pm\rangle$ state at zero magnetic fields. Rabi oscillation can be observed in the optical signal due to the microwave drive, see Fig. 3b. In Fig. 3c, we depict the magnetic field dependence of the resonance signal. As the magnetic field enhances the zero-field mixing of the $m_S = \pm 1$ states reduces; the states become the eigenstates of the Zeeman Hamiltonian term, and eventually depend linearly on the magnetic field. On the other hand, as can be seen in Fig. 3c, the spin states are independent of the magnetic field in first order at $B \approx 0$. The zero first-order Zeeman (ZEFOZ) transitions arising at this field are protected from magnetic fluctuations that result in an elongated coherence time of the qubit states. We study this effect through the magnetic field dependence of the free induction decay time ($T_2^\star$) in Fig. 3d. As can be seen, the coherence time is enhanced by a factor of 7.5 at $B = 0$ and reaches a value as high as 128 ns. Note that the coherence time may be further elongated by driving a transition between $|+\rangle$ and $|-\rangle$ states with a parallel to plane-polarized microwave field. These coherence protection schemes are indispensable in hBN as it possesses nuclear spins in its lattice with 100% natural abundance. We note furthermore that the electron spin resonance linewidth is reduced by a factor of 4.2 at zero magnetic fields, see Fig. 3e.

Note, furthermore, that the magnetic resonance map in Fig. 3c exhibits a broad driving frequency-independent signal at $B \approx 160$ G. This signal is due to hyperfine coupling of the environment whose effect is enhanced at the avoided-crossing of the ground state spin levels observed at $B \approx 160$ G, see Supplementary Note 5. The interplay of the optical pumping and the strong hyperfine coupling at this magnetic field may give rise to efficient polarization of the surrounding spin bath. Low magnetic field hyperpolarization of an hBN sample can be utilized in sensitivity-

enhanced NMR and MRI measurements[35].

**VB2 as a sensor.** Finally, we study the sensitivity of the VB2 center. To this end, we first determine the pressure and electric field dependence of the ZFS parameters, for which we obtain $d\widetilde{D}/dp = 9.98$ MHz/kBar (-8.61 MHz/kBar) and $d\widetilde{E}/dp = 8.50$ MHz/kBar (-9.36 MHz/kBar) for pressure applied parallel (perpendicular) to the $V_B$-$V_N$ axis and $d\widetilde{D}/d\mathcal{E} = 0.04$ Hz cm/V (-3.45 Hz cm/V) and $d\widetilde{E}/d\mathcal{E} = 3.81$ Hz cm/V (7.52 Hz cm/V) for static electric field $\mathcal{E}$ set parallel (perpendicular) to the $V_B$-$V_N$ axis. The stress coupling parameters of the VB2 center and the $V_B$ center[29] are comparable, however, they are two orders of magnitude larger than the NV center's stress coupling parameter[36]. The electric field coupling parameter of the VB2 center along special directions is comparable to the NV center's electric field coupling strength.

The shot noise limited sensitivity of a single VB2 sensor in continuous wave magnetic resonance measurement scheme can be obtained according to the formula[37,38]

$$\eta_{\mathrm{MR}} = \left(\frac{d\nu_{0+}}{d\mathcal{P}}\right)^{-1} \frac{\Delta\nu}{C\sqrt{\mathcal{R}}}, \tag{1}$$

where $\nu_{0+}$ is the resonance frequency, $\mathcal{P}$ is the perturbation to be measured, $\Delta\nu$ is the full width at half maximum of the magnetic resonance curve, which takes 49.5 MHz at zero magnetic fields for electric field, pressure, and temperature sensing and 205 MHz at high magnetic field values for DC magnetic field sensing, $C \approx 0.05$ is the estimated spin read-out contrast, and $\mathcal{R}$ is the photon count that may reach 100 kcps in saturation. Using this formula and the values specified above, for pressure, DC electric field, and DC magnetic field sensitivity we respectively obtain 30 MPa/Hz$^{1/2}$, 907 kV/cm/Hz$^{1/2}$, and 463 $\mu$T/Hz$^{1/2}$ for a single VB2 defect in hBN in continuous wave sensing mode.

**Observation of the VB2 center in single layer hBN.** The VB2 configuration is directly observed in our measurements using ADF-STEM imaging of a single layer free-standing hBN sample, see Fig. 4a. The image of the VB2 configuration resembles the boron vacancy-nitrogen vacancy complex, however, the intensity profile across the bright atoms shows an excellent match to the VB2 complex with an N atom contrast from one of the B atom sites, see the multi-slice simulated STEM image in Fig. 4b. We note that the appearance of the VB2 configuration is a direct consequence of

the STEM measurement itself. In our measurements, a nearly defect-free hBN layer is suspended on a metallic grid. As the electron beam scans through the sample defects, more likely boron vacancies are created.[39] Prior work showed that electron beam irradiation of monolayer hBN causes the ejection of B and N atoms around point defects. A variety of point defects including the VB2 defect is produced. We note also that high positioning accuracy may be achieved in defect fabrication in STEM by using focused electron beam pulses at specific points instead of scanning the surface.[39]

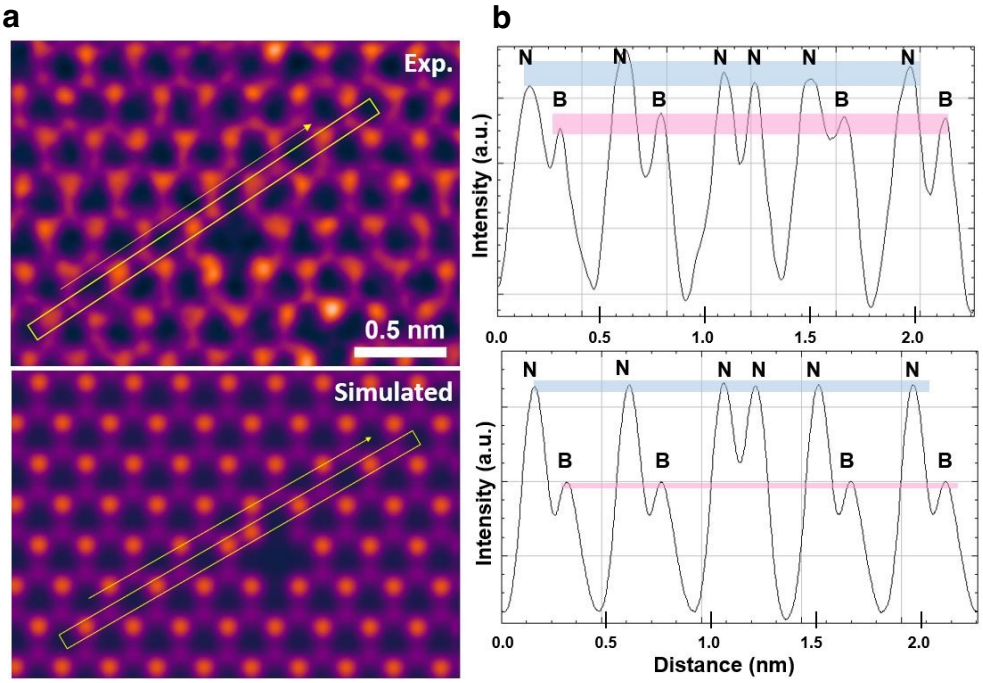


Figure 4: **Scanning tunneling electron microscope image of the VB2 center.** **a**, A false-colored ADF-STEM image of the VB2 configuration in single layer free-standing hBN sample. The top and bottom panels show the experiment and simulation. **b**, Intensity profile across the bright atoms along the yellow dashed box in **a** that reveals an anti-site nitrogen next to the vacancy sites.

## Discussion

The sensitivity of the VB2 center in a continuous wave measurement scheme is expected to be lower than that of the NV center in diamond, dominantly due to the enhanced magnetic resonance

linewidth and the slightly lower photon count of the VB2 center. On the other hand, it may still be useful for high spatial resolution sensing in near-surface and low-dimension applications. The dipole-allowed optical transition, the sizable spin read-out contrast, and the narrowed-down magnetic resonance signal at zero magnetic fields are all in favor of the VB2 center.

Pulsed sensing protocols and decoherence protection techniques can be utilized to enhance the sensitivity of the VB2 center further. The low symmetric structure offers new functionalities. The long-lived bright singlet manifold can be utilized as a memory and may lead to the storage of spin state population information beyond the spin relaxation time of the ground state triplet. This may be utilized in a single-shot read-out of the spin states when the center is coupled with an optical cavity. Furthermore, dressing of the $|\pm\rangle$ states with resonant microwave drive may be used in filtering out low-frequency magnetic field fluctuations[40] that can give rise to a highly protected subspace in hBN.

Fabrication of point defect qubits in 2D materials offers new possibilities in nanometer-scale sensing. For example, few-layer hBN samples with pre-fabricated sensors may be moved on top of nano-scale structures or installed in van der Waals heterostructure in order to obtain high spatial resolution information not accessible with other means. The VB2 center exhibiting desirable qubit properties has already been fabricated in single-layer hBN providing a suitable sensor for such applications.

## Summary

In summary, we investigated the peculiar properties of the VB2 center directly observed in our STEM measurements in a free-standing single sheet of hexagonal boron nitride. We showed that the triplet ground state of the VB2 defect implements an optically addressable spin qubit with novel characteristics. The possibility of an efficient coherence protection mechanism and dipole-allowed optical transition makes the VB2 center a suitable candidate for emerging point defect qubit applications, such as sub-nanoscale sensing in van der Waals heterostructure.

## Methodology

In this study, we use scanning transmission electron microscopy, three state-of-the-art electronic structure computational methods, see Supplementary Note 1, and exact spin dynamics simulations to investigate the VB2 defect.

**Sample and STEM measurements.** The hBN film was spin-coated with PMMA, etched in ammonium borane to remove the Cu, and then transferred to a TEM grid. The PMMA was removed by acetone overnight and then the samples were annealed in vacuum overnight. Annular dark-field scanning transmission electron microscopy (ADF-STEM) was performed using a JEOL ARM200CF STEM equipped with a CEOS probe corrector operated at an accelerating voltage of 80 kV. ADF-STEM with a low collection angle was acquired to increase the signal from light elements and discriminate B and N atoms as darker and brighter contrast. Dwell times of 5-20 $\mu$s and a pixel size of 0.006 nm px-1 were used for imaging with a convergence semi-angle of 22.5 mrad and a beam current of 35 pA. A camera length of 20 cm was used to provide a large collection of low-angle scattered electrons, increasing the contrast of hBN. ImageJ was used for line profile measurements and image analysis. Multislice image simulations were using QSTEM software with an accelerating voltage of 80 kV, a convergence semiangle of 21 mrad, a detector angle of 40-110 mrad, a spherical aberration of 0.001 nm, the chromatic aberration of 1 mm, and the defocus of -0.001 nm. The ADF-STEM images were colorized with Gem in lookup tables using ImageJ for better visibility.

**DFT calculations.** We apply density functional theory (DFT) calculations to study the energetic, ground state electronic, and spin properties, as well as the selected excited state properties of the VB2 defect. Throughout this work, we use a plane wave basis set of 450 eV and PAW [41] core potentials as implemented in VASP[42] and HSE06 hybrid exchange-correlation functional[43] with 0.32 exact exchange fraction[44]. For the charge transition level calculations we use a 768-atom supercell model of bulk hBN and the charge correction scheme by Freysoldt et al.[45]. For all the other calculations, we use a 162-atom single-sheet model of hBN embedding a single defect complex. In perpendicular direction, we use 30 Å supercell size. Furthermore, in single-layer calculations, we use DFT-D3 correction method of Grimme et al.[46]. We use a ZFS tensor calculation routine in

the PAW formalism as implemented in VASP and spin contamination error correction as proposed in Ref. [[47]]. We note that the spin contamination error is comparable with the largest element of the ZFS tensor, thus accurate ZFS parameters can only be achieved after decontamination. The DFT values are confirmed by NEVPT2 results for the unstrained configuration.

**NEVPT2 calculations.**

The N-Electron Valence State Perturbation Theory (NEVPT2)[48] calculations were carried out using cc-pVDZ basis set[49] by the ORCA program package[50]. To this end, we employed a flake model of hBN, consisting of 38 B-, 40 N-, and 22 H-atoms. The underlining complete active space self-consistent field (CASSCF) calculations were performed based on the unrestricted Hartree-Fock orbitals, while we employed the CAS of 8 electrons and 8 orbitals and considered 6 triplet and 6 singlet states for the state-averaging. The spin-orbit coupling was introduced in the framework of quasi-degenerate perturbation theory, as implemented in ORCA.

**DMRG calculations.** DMRG [51] is a reference-free variational post-Hartree–Fock method which relies on an iterative local optimization scheme based on Schmidt decomposition. [52] The method is natively suitable for describing multireference problems of several dozens of strongly correlated orbitals. [53,54] As DMRG is capable of treating significantly larger completely active spaces compared to CASSCF-based methods, it can provide more robust results for strongly correlated problems.

DMRG computations are performed applying the Budapest DMRG package [55] restricting the spin of the target states to 0 and 1. In the DMRG truncation, [54] the density matrix is formed of the equally weighted linear combination of the targeted spin-states, and the quantum information loss is preferred to be kept below threshold value $\chi = 10^{-5}$. Considering that only six defect orbitals display multireference character whereas the rest of the orbitals are found to be contributing to the dynamical correlation effects, a variant of the standard dynamically extended active space approach (DEAS)[56] is implemented and applied to initialize environment DMRG block states. Namely, the orbitals in the DMRG chain are arranged according to their localization on the defect atoms in descending order and the DMRG system block is optimized in the configuration space of the en-

vironment orbitals which is composed of determinants allowing up to all single orbital excitations. Contrary to the standard DEAS implementation, where environment block states tend to capture the essence of the multireference features of the corresponding orbitals, the modified initialization scheme focuses on the description of dynamical correlations of the complete environment from the initial DMRG micro iterations. The application of the novel DEAS protocol is favorable for the particular orbital space setups of current interest, i.e., orbitals display well-distinguished static or dynamical correlation character. In practice, the relative vertical energies are found to approach convergence within the first macro iterations of DMRG owing to the effective environmental initialization.

The input required for the DMRG calculations, i.e., Hamiltonian matrix elements, are expanded in the active space of Kohn-Sham DFT orbitals using program suite ORCA [57]. The spin-restricted Kohn-Sham orbitals are obtained assuming PBE correlation-exchange functional and fixing half-occupation on the highest-lying valence defect orbital pair. Matrix elements were computed by MRCC program [58,59] applying the complete active space protocol [60,61]. In our analysis, various active space setups were tested providing consistent excitation spectra, while the actual results are presented for 100 canonical orbitals filled with 188 electrons. The NEVPT and the DMRG calculations were performed on the same flake geometry.

**Spin dynamics simulations.** Exact spin dynamics simulations were carried out by using a spin Hamiltonian parametrized by our DFT spin coupling parameter calculations[62]. Magnetic resonance (MR) spectra were obtained by propagating the states of a four-spin model, including the triplet electron spin and three closest $^{14}$N triplet nuclear spins, under an oscillating magnetic field of various frequencies and polarization direction. The MR figures show the change of the initial population of the $m_{\mathrm{S}} = \pm 1$ states. The $T_2^\star$ coherence time was obtained by simulating the coherent oscillation of 178 electron spin-nuclear spin two spin systems. The overall coherence function is obtained as a product of the individual coherence functions.[63] The decaying coherence function of the electron spin was fitted by a Gaussian function to obtain the $T_2^\star$. No nuclear spin nuclear spin flip-flops are included here.

## Data availability

The data that support the findings of this study are available from the authors upon reasonable request.


## Acknowledgments

This research was supported by the National Research, Development, and Innovation Office of Hungary within the Quantum Information National Laboratory of Hungary (Grant No. 2022-2.1.1-NL-2022-00004) and within grants FK 135496 and FK 145395. We acknowledge support from the Knut and Alice Wallenberg Foundation through WBSQD2 project (Grant No. 2018.0071). Support from the Swedish Government Strategic Research Area SeRC and the Swedish Government Strategic Research Area in Materials Science on Functional Materials at Linköping University (Faculty Grant SFO-Mat-LiU No. 2009 00971) is gratefully acknowledged. A.G. acknowledges the Hungarian NKFIH grants No. KKP129866 of the National Excellence Program of Quantum-coherent materials project, and the NKFIH through the National Quantum Technology Program (Grant No. 2017-1.2.1-NKP-2017-00001) and the Quantum Information National Laboratory sponsored by Ministry of Innovation and Technology of Hungary. Ö.L. acknowledges financial support from the Hungarian National Research, Development and Innovation Office (NKFIH) through Grants No. K134983, TKP2021-NVA-04, Quantum Information National Laboratory of Hungary, the Hans Fischer Senior Fellowship programme funded by the Technical University of Munich Institute for Advanced Study, and the Center for Scalable and Predictive methods for Excitation and Correlated phenomena (SPEC), which is funded as part of the Computational Chemical Sciences Program by the U.S. Department of Energy (DOE), Office of Science, Office of Basic Energy Sciences, Division of Chemical Sciences, Geosciences, and Biosciences at Pacific Northwest National Laboratory. A.P. and G.T. were supported by the János Bolyai Research Scholarship of the Hungarian Academy of Sciences. G.T. also acknowledges the ÚNKP-20-5 New National Excellence Program for Ministry Innovation and Technology from the source of the National Research, Development and Innovation Fund. The computations were enabled by resources provided by the National Academic Infrastructure for Supercomputing in Sweden (NAISS) and the Swedish National In-

frastructure for Computing (SNIC) at the National Supercomputer Centre (NSC) partially funded by the Swedish Research Council through grant agreements no. 2022-06725 and no. 2018-05973. We acknowledge KIFÜ for awarding us access to computational resources based in Hungary.

## Author contributions

The DFT calculations were performed by R.B., V.I., O.B.L. , and G.T. with inputs from A.G. and I.A.A. The DFT-CAS-DMRG and NEVPT2 calculations were performed by G.B. and A.P. , respectively, with inputs from V.I. , A.G., and Ö.L. The STEM measurements were carried out by H.P. and J. H. W. The spin dynamics simulations were carried out by V.I. The results were analyzed with contributions from all authors. V.I. wrote the manuscript with inputs from the coauthors.

## Competing interests

The authors declare no competing interests.

## References

1. Degen, C., Reinhard, F. & Cappellaro, P. Quantum sensing. *Reviews of Modern Physics* **89**, 035002 (2017). URL https://link.aps.org/doi/10.1103/RevModPhys.89.035002. Publisher: American Physical Society.

2. Doherty, M. W. *et al.* The nitrogen-vacancy colour centre in diamond. *Physics Reports* **528**, 1 – 45 (2013). URL http://www.sciencedirect.com/science/article/pii/S0370157313000562.

3. Taylor, J. M. *et al.* High-sensitivity diamond magnetometer with nanoscale resolution. *Nature Physics* **4**, 810–816 (2008). URL https://www.nature.com/articles/nphys1075. Number: 10 Publisher: Nature Publishing Group.

4. Michl, J. *et al.* Robust and Accurate Electric Field Sensing with Solid State Spin Ensembles. *Nano Letters* **19**, 4904–4910 (2019). URL

https://doi.org/10.1021/acs.nanolett.9b00900. Publisher: American Chemical Society.

5. Ovartchaiyapong, P., Lee, K. W., Myers, B. A. & Jayich, A. C. B. Dynamic strain-mediated coupling of a single diamond spin to a mechanical resonator. *Nature Communications* **5**, 4429 (2014). URL https://www.nature.com/articles/ncomms5429. Number: 1 Publisher: Nature Publishing Group.

6. Kucsko, G. *et al.* Nanometre-scale thermometry in a living cell. *Nature* **500**, 54–58 (2013). URL https://doi.org/10.1038/nature12373.

7. DeVience, S. J. *et al.* Nanoscale NMR spectroscopy and imaging of multiple nuclear species. *Nature Nanotechnology* **10**, 129–134 (2015). URL https://www.nature.com/articles/nnano.2014.313. Number: 2 Publisher: Nature Publishing Group.

8. Bucher, D. B. *et al.* Quantum diamond spectrometer for nanoscale NMR and ESR spectroscopy. *Nature Protocols* **14**, 2707–2747 (2019). URL https://www.nature.com/articles/s41596-019-0201-3. Number: 9 Publisher: Nature Publishing Group.

9. Schmitt, S. *et al.* Submillihertz magnetic spectroscopy performed with a nanoscale quantum sensor. *Science* **356**, 832–837 (2017). URL https://science.sciencemag.org/content/356/6340/832.

10. Boss, J. M., Cujia, K. S., Zopes, J. & Degen, C. L. Quantum sensing with arbitrary frequency resolution. *Science* **356**, 837–840 (2017). URL https://science.sciencemag.org/content/356/6340/837. Publisher: American Association for the Advancement of Science Section: Reports.

11. Lovchinsky, I. *et al.* Nuclear magnetic resonance detection and spectroscopy of single proteins using quantum logic. *Science* **351**, 836–841 (2016). URL

https://science.sciencemag.org/content/351/6275/836. Publisher: American Association for the Advancement of Science Section: Report.

12. Bluvstein, D., Zhang, Z., McLellan, C. A., Williams, N. R. & Jayich, A. C. B. Extending the quantum coherence of a near-surface qubit by coherently driving the paramagnetic surface environment. *Phys. Rev. Lett.* **123**, 146804 (2019). URL https://link.aps.org/doi/10.1103/PhysRevLett.123.146804.

13. Tetienne, J.-P. Quantum sensors go flat. *Nature Physics* 1–2 (2021). URL https://www.nature.com/articles/s41567-021-01338-5. Bandiera_abtest: a Cg_type: Nature Research Journals Primary_atype: News & Views Publisher: Nature Publishing Group Subject_term: Qubits;Two-dimensional materials Subject_term_id: qubits;two-dimensional-materials.

14. Vaidya, S., Gao, X., Dikshit, S., Aharonovich, I. & Li, T. Quantum sensing and imaging with spin defects in hexagonal boron nitride **8**, 2206049. URL https://doi.org/10.1080/23746149.2023.2206049. Publisher: Taylor & Francis _eprint: https://doi.org/10.1080/23746149.2023.2206049.

15. Kumar, P. *et al.* Magnetic imaging with spin defects in hexagonal boron nitride **18**, L061002. URL https://link.aps.org/doi/10.1103/PhysRevApplied.18.L061002. Publisher: American Physical Society.

16. Healey, A. J. *et al.* Quantum microscopy with van der waals heterostructures 1–5. URL https://www.nature.com/articles/s41567-022-01815-5. Publisher: Nature Publishing Group.

17. Robertson, I. O. *et al.* Detection of paramagnetic spins with an ultrathin van der waals quantum sensor **17**, 13408–13417. URL https://doi.org/10.1021/acsnano.3c01678. Publisher: American Chemical Society.

18. Gao, X. *et al.* Quantum sensing of paramagnetic spins in liquids with spin qubits in hexagonal boron nitride **10**, 2894–2900. URL

https://doi.org/10.1021/acsphotonics.3c00621. Publisher: American Chemical Society.

19. Sasaki, K. *et al.* Magnetic field imaging by hBN quantum sensor nanoarray **122**, 244003. URL https://doi.org/10.1063/5.0147072.

20. Exarhos, A. L., Hopper, D. A., Patel, R. N., Doherty, M. W. & Bassett, L. C. Magnetic-field-dependent quantum emission in hexagonal boron nitride at room temperature. *Nature Communications* **10**, 222 (2019). URL https://www.nature.com/articles/s41467-018-08185-8. Number: 1 Publisher: Nature Publishing Group.

21. Gottscholl, A. *et al.* Initialization and read-out of intrinsic spin defects in a van der Waals crystal at room temperature. *Nature Materials* **19**, 540–545 (2020). URL https://www.nature.com/articles/s41563-020-0619-6. Number: 5 Publisher: Nature Publishing Group.

22. Stern, H. L. *et al.* Room-temperature optically detected magnetic resonance of single defects in hexagonal boron nitride **13**, 618. URL https://www.nature.com/articles/s41467-022-28169-z. Number: 1 Publisher: Nature Publishing Group.

23. Stern, H. L. *et al.* A quantum coherent spin in a two-dimensional material at room temperature. URL http://arxiv.org/abs/2306.13025. 2306.13025 [cond-mat, physics:quant-ph].

24. Ivády, V. *et al.* Ab initio theory of the negatively charged boron vacancy qubit in hexagonal boron nitride. *npj Computational Materials* **6**, 1–6 (2020). URL https://www.nature.com/articles/s41524-020-0305-x. Number: 1 Publisher: Nature Publishing Group.

25. Sajid, A., Thygesen, K. S., Reimers, J. R. & Ford, M. J. Edge effects on optically detected magnetic resonance of vacancy defects in hexagonal boron nitride. *Communications Physics* **3**,

1–8 (2020). URL https://www.nature.com/articles/s42005-020-00416-z. Number: 1 Publisher: Nature Publishing Group.

26. Reimers, J. R. *et al.* Photoluminescence, photophysics, and photochemistry of the $V_B^-$ defect in hexagonal boron nitride. *Phys. Rev. B* **102**, 144105 (2020). URL https://link.aps.org/doi/10.1103/PhysRevB.102.144105.

27. Gottscholl, A. *et al.* Room temperature coherent control of spin defects in hexagonal boron nitride. *Science Advances* **7**, eabf3630 (2021). URL https://advances.sciencemag.org/content/7/14/eabf3630. Publisher: American Association for the Advancement of Science Section: Research Article.

28. Liu, W. *et al.* Rabi oscillation of V$_\text{B}^-$ spin in hexagonal boron nitride. *arXiv:2101.11220 [quant-ph]* (2021). URL http://arxiv.org/abs/2101.11220. ArXiv: 2101.11220.

29. Gottscholl, A. *et al.* Spin defects in hBN as promising temperature, pressure and magnetic field quantum sensors. *Nature Communications* **12**, 4480 (2021). URL https://www.nature.com/articles/s41467-021-24725-1. Bandiera_abtest: a Cc_license_type: cc_by Cg_type: Nature Research Journals Number: 1 Primary_atype: Research Publisher: Nature Publishing Group Subject_term: Electronic properties and materials;Qubits Subject_term_id: electronic-properties-and-materials;qubits.

30. Gottscholl, A. *et al.* Sub-nanoscale Temperature, Magnetic Field and Pressure sensing with Spin Centers in 2D hexagonal Boron Nitride. *arXiv:2102.10890 [cond-mat, physics:quant-ph]* (2021). URL http://arxiv.org/abs/2102.10890. ArXiv: 2102.10890.

31. Strand, J., Larcher, L. & Shluger, A. L. Properties of intrinsic point defects and dimers in hexagonal boron nitride. *Journal of Physics: Condensed Matter* **32**, 055706 (2019). URL https://doi.org/10.1088/1361-648x/ab4e5d.

32. Li, K., Smart, T. J. & Ping, Y. Carbon trimer as a 2 eV single-photon emitter candidate in hexagonal boron nitride: A first-principles study **6**, L042201. URL

https://link.aps.org/doi/10.1103/PhysRevMaterials.6.L042201. Publisher: American Physical Society.

33. Vogl, T., Lu, Y. & Lam, P. K. Room temperature single photon source using fiber-integrated hexagonal boron nitride. *Journal of Physics D: Applied Physics* **50**, 295101 (2017). URL https://doi.org/10.1088/1361-6463/aa7839. Publisher: IOP Publishing.

34. Li, X., Scully, R. A., Shayan, K., Luo, Y. & Strauf, S. Near-Unity Light Collection Efficiency from Quantum Emitters in Boron Nitride by Coupling to Metallo-Dielectric Antennas. *ACS Nano* **13**, 6992–6997 (2019). URL https://doi.org/10.1021/acsnano.9b01996. Publisher: American Chemical Society.

35. Bucher, D. B., Glenn, D. R., Park, H., Lukin, M. D. & Walsworth, R. L. Hyperpolarization-Enhanced NMR Spectroscopy with Femtomole Sensitivity Using Quantum Defects in Diamond. *Physical Review X* **10**, 021053 (2020). URL https://link.aps.org/doi/10.1103/PhysRevX.10.021053. Publisher: American Physical Society.

36. Udvarhelyi, P., Shkolnikov, V. O., Gali, A., Burkard, G. & Pályi, A. Spin-strain interaction in nitrogen-vacancy centers in diamond. *Phys. Rev. B* **98**, 075201 (2018). URL https://link.aps.org/doi/10.1103/PhysRevB.98.075201.

37. Dréau, A. *et al.* Avoiding power broadening in optically detected magnetic resonance of single NV defects for enhanced dc magnetic field sensitivity. *Physical Review B* **84**, 195204 (2011). URL https://link.aps.org/doi/10.1103/PhysRevB.84.195204.

38. Pham, L. M. Magnetic Field Sensing with Nitrogen-Vacancy Color Centers in Diamond (2013). URL https://dash.harvard.edu/handle/1/11051173. Accepted: 2013-09-18T14:29:19Z.

39. Park, H. *et al.* Atomically Precise Control of Carbon Insertion into hBN Monolayer Point Vacancies using a Focused Electron Beam Guide. *Small* **17**, 2100693 (2021). URL

https://onlinelibrary.wiley.com/doi/abs/10.1002/smll.202100693. _eprint: https://onlinelibrary.wiley.com/doi/pdf/10.1002/smll.202100693.

40. Miao, K. C. *et al.* Universal coherence protection in a solid-state spin qubit. *Science* **369**, 1493–1497 (2020). URL https://science.sciencemag.org/content/369/6510/1493.

41. Blöchl, P. E. Projector augmented-wave method. *Phys. Rev. B* **50**, 17953–17979 (1994). URL http://link.aps.org/doi/10.1103/PhysRevB.50.17953.

42. Kresse, G. & Hafner, J. ¡i¿ab initio¡/i¿ molecular-dynamics simulation of the liquid-metal–amorphous-semiconductor transition in germanium. *Phys. Rev. B* **49**, 14251–14269 (1994). URL http://link.aps.org/doi/10.1103/PhysRevB.49.14251.

43. Heyd, J., Scuseria, G. E. & Ernzerhof, M. Hybrid functionals based on a screened coulomb potential. *J. Chem. Phys.* **118**, 8207 (2003). URL http://dx.doi.org/10.1063/1.1564060.

44. Weston, L., Wickramaratne, D., Mackoit, M., Alkauskas, A. & Van de Walle, C. G. Native point defects and impurities in hexagonal boron nitride. *Phys. Rev. B* **97**, 214104 (2018). URL https://link.aps.org/doi/10.1103/PhysRevB.97.214104.

45. Freysoldt, C., Neugebauer, J. & Van de Walle, C. G. Fully *Ab Initio* finite-size corrections for charged-defect supercell calculations. *Phys. Rev. Lett.* **102**, 016402 (2009). URL http://link.aps.org/doi/10.1103/PhysRevLett.102.016402.

46. Grimme, S., Antony, J., Ehrlich, S. & Krieg, H. A consistent and accurate ab initio parametrization of density functional dispersion correction (dft-d) for the 94 elements h-pu. *The Journal of Chemical Physics* **132**, 154104 (2010). URL https://doi.org/10.1063/1.3382344. https://doi.org/10.1063/1.3382344.

47. Biktagirov, T., Schmidt, W. G. & Gerstmann, U. Spin decontamination for magnetic dipolar coupling calculations: Application to high-spin molecules and solid-state spin qubits. *Physical Review Research* **2**, 022024 (2020). URL https://link.aps.org/doi/10.1103/PhysRevResearch.2.022024. Publisher: American Physical Society.

48. Angeli, C., Cimiraglia, R., Evangelisti, S., Leininger, T. & Malrieu, J.-P. Introduction of n-electron valence states for multireference perturbation theory. *The Journal of Chemical Physics* **114**, 10252–10264 (2001). URL https://aip.scitation.org/doi/10.1063/1.1361246. Publisher: American Institute of Physics.

49. Dunning, T. H. Gaussian basis sets for use in correlated molecular calculations. I. The atoms boron through neon and hydrogen. *The Journal of Chemical Physics* **90**, 1007–1023 (1989). URL https://aip.scitation.org/doi/10.1063/1.456153. Publisher: American Institute of Physics.

50. Neese, F. Software update: the orca program system, version 4.0. *Wiley Interdisciplinary Reviews: Computational Molecular Science* **8**, e1327 (2018).

51. White, S. R. & Martin, R. L. Ab initio quantum chemistry using the density matrix renormalization group. *The Journal of Chemical Physics* **110**, 4127–4130 (1999). URL https://doi.org/10.1063/1.478295. https://doi.org/10.1063/1.478295.

52. Schollwöck, U. The density-matrix renormalization group. *Rev. Mod. Phys.* **77**, 259–315 (2005). URL https://link.aps.org/doi/10.1103/RevModPhys.77.259.

53. Olivares-Amaya, R. *et al.* The ab-initio density matrix renormalization group in practice. *J. Chem. Phys.* **142** (2015). URL https://aip.scitation.org/doi/10.1063/1.4905329.

54. Szalay, Sz. *et al.* Tensor product methods and entanglement optimization for ab initio quantum chemistry. *Int. J. Quantum Chem.* **115**, 1342–1391 (2015). URL http://dx.doi.org/10.1002/qua.24898.

55. Legeza, Ö., Veis, L. & Mosoni, T. QC-DMRG-Budapest, a program for quantum chemical DMRG calculations (2020).

56. Legeza, O. & Sólyom, J. Optimizing the density-matrix renormalization group method using quantum information entropy. *Phys. Rev. B* **68**, 195116 (2003). URL https://link.aps.org/doi/10.1103/PhysRevB.68.195116.

57. Neese, F. The orca program system. *Wiley Interdiscip. Rev.: Comput. Mol. Sci.* **2**, 73–78 (2012). URL https://onlinelibrary.wiley.com/doi/abs/10.1002/wcms.81.

58. Kallay, M. *et al.* Mrcc, a quantum chemical program suite (2020). URL www.mrcc.hu.

59. Kallay, M. *et al.* The mrcc program system: Accurate quantum chemistry from water to proteins. *J. Chem. Phys.* **152**, 074107 (2020). URL https://doi.org/10.1063/1.5142048.

60. Jensen, F. *Introduction to Computational Chemistry* (John Wiley and Sons, Inc., Hoboken, NJ, USA, 2006).

61. Barcza, G. *et al.* DMRG on Top of Plane-Wave Kohn-Sham Orbitals: A Case Study of Defected Boron Nitride. *J Chem Theory Comput* **17**, 1143–1154 (2021).

62. Ivády, V., Abrikosov, I. A. & Gali, A. First principles calculation of spin-related quantities for point defect qubit research. *npj Computational Materials* **4**, 76 (2018). URL https://doi.org/10.1038/s41524-018-0132-5.

63. Seo, H. *et al.* Quantum decoherence dynamics of divacancy spins in silicon carbide. *Nature Communications* **7**, 1–9 (2016). URL

https://www.nature.com/articles/ncomms12935. Number: 1 Publisher: Nature Publishing Group.